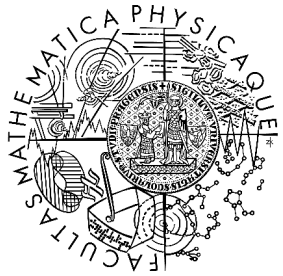

FACULTY
OF MATHEMATICS
AND PHYSICS
Charles University

BACHELOR THESIS

Petra Hrubcová

Visualization of superfluid helium flows in the proximity of boundaries

Department of Low Temperature Physics

Supervisor of the bachelor thesis: Dr. Marco La Mantia, Ph.D.

Study programme: Physics

Study branch: General Physics

Prague 2018

I declare that I carried out this bachelor thesis independently, and only with the cited sources, literature and other professional sources.

I understand that my work relates to the rights and obligations under the Act No. 121/2000 Sb., the Copyright Act, as amended, in particular the fact that the Charles University has the right to conclude a license agreement on the use of this work as a school work pursuant to Section 60 subsection 1 of the Copyright Act.

In ..... date ..... signature of the author

Title
Visualization of superfluid helium flows in the proximity of boundaries

Author
Petra Hrubcová

Department
Department of Low Temperature Physics

Supervisor
Dr. Marco La Mantia, Ph.D., Department of Low Temperature Physics

Abstract
The investigation of superfluid helium (He II) flows is an active and challenging research field. Progress in our phenomenological understanding of the underlying physics has been achieved in recent years by employing flow visualization techniques that allow following the motion of relatively small particles suspended in the fluid. The flow-induced particle behaviour is studied in the case of thermal counterflow – the most common type of He II flow – close to the flow source, where a significant vorticity enhancement is observed. The work aim is therefore to give a significant contribution to the emerging line of scientific enquiry dedicated to the study of wall-bounded quantum flows.

Keywords
low temperature physics • superfluidity • quantum turbulence • flow visualization • boundary layer theory

Firstly, I would like to thank my supervisor, Dr. Marco La Mantia, Ph.D., for his excellent guidance when preparing this work. I am also thankful to my colleagues Mgr. Patrik Švančara and RNDr. Daniel Duda, Ph.D. for their contributions to the performed experiments. Finally, I thank my parents for their unlimited support in my studies.

Contents

Introduction

At the beginning of the 20^{th} century everything in physics seemed to be understood. Then came all the big experiments (e.g. Rutherford's experiment or Stern-Gerlach experiment) and physics has divided into several branches studying specific conditions (high energies, high magnetic fields, low temperatures etc). Investigating systems in these extreme conditions reveals phenomena unimaginable from the classical point of view. For low temperature physics everything started with the liquefaction of gases through the reverse Joule-Thompson effect at the end of 19^{th} century [1]. After 30 years of efforts, the only gaseous substance remaining was helium. This milestone was reached in 1908. On 10 June the Dutch physicist Heike Kamerlingh Onnes liquefied helium in his laboratory in Leiden.

Helium becomes liquid below 4.2 K, at the saturated vapour pressure. Its properties however are very different from other liquids as it stays liquid to absolute zero. Its liquid phase also experiences a second order phase transition (called λ transition). Below the transition temperature we refer to the liquid as superfluid helium or He II, the liquid above the transition temperature is referred as He I.

Flows of He I can be described by the Navier-Stokes equation and He I behaves as a classical viscous fluid. The uniqueness of ^{4}He appears for He II, where we can observe flows without any inner friction. This property, called superfluidity, leads to intriguing phenomena, such as thermally driven counterflow, quantum turbulence and temperature waves.

In order to describe such a behaviour of He II, Tisza and Landau [2] developed the phenomenological two-fluid model. They assumed that the fluid consists of two components, one viscous, the normal fluid, and the other inviscid, the superfluid component. For low temperatures, we can also consider quantum effects. This results in the presence of quantized vortices in the superfluid component. They are linear singularities in the otherwise smooth wave function and the circulation

around them is quantized. The alignment of quantized vortices depends on the type of flow that causes them and for special cases it can result in quantum turbulence.

Many new techniques had to be developed or adjusted to enable research in low temperatures. Phenomenological behaviour can be studied e.g. by visualization of the flow. It enables direct observation of the flow by using solidified particles that are distributed in the volume of interest, illuminated by a laser sheet and their motion is recorded by a high-frequency camera. The motions of the particles are influenced by the flow and hence give us information about the fluid flow. The particles can be made, for example, of hydrogen or deuterium.

In this work the particle tracking velocimetry technique was used to analyse the motion of the particles suspended in the liquid and we were able to estimate the statistical distributions of the particle velocities.

The aim of the experiment discussed below is to compare the flow-induced particle behaviour in the boundary proximity to that seen in the bulk, i.e., as far away as possible from the walls. Indeed, to this day, boundary layers in superfluids were given little attention and there is especially a lack of relevant experimental studies, see, e.g., [3] and references therein.

We studied a special type of flow, that exists only in He II, called counterflow, where the two components flow in opposite directions. The source of this flow is a heater. We investigated the behaviour of ^{4}He in the proximity of the boundary created by the heater in a closed channel.

1 Theoretical Part

1.1 Liquid Helium

Helium has two stable isotopes – the naturally occurring ^{4}He and the much more rare ^{3}He. They only differ in the number of neutrons in their nuclei: ^{4}He has 2 neutrons and ^{3}He only 1. As they are both in the noble gas section of the periodic table, their interaction with other matter is mainly through the Van der Waals force, which is a weak force. Hence we can consider them to be almost ideal monoatomic gases. Although at room temperature they are almost indistinguishable in terms of the collective behaviour, when we reach low temperatures, their properties differ quite significantly. ^{4}He acts as a boson (due to its spherical symmetry and zero spin) and hence follows the Bose–Einstein statistics, while ^{3}He represents a fermionic system, ruled by the Fermi–Dirac description. In this thesis we will concentrate on ^{4}He only.

Phase Diagram

The typical phase diagram of an ordinary substance has two significant points – the critical point and the triple point, which marks the co-existence of solid, liquid and gas phases. In the case of ^{4}He, the critical point can be found at very low temperatures, compared to other materials, that is at temperature $T_c \approx 5.2\,\mathrm{K}$ and pressure $P_c \approx 0.225\,\mathrm{MPa}$, as shown in figure 1.1. Additionally, ^{4}He has no triple point. As a result, ^{4}He is in its liquid phase down to absolute zero unless we increase the pressure to about 2.5 MPa.

In addition to ordinary phases (gaseous, liquid, solid), ^{4}He has other phases. When Onnes and Dana were cooling down helium in 1908 [4], they noticed that around 2 K the boiling of the liquid stopped. They investigated the fluid properties around this temperature more carefully and found out that the temperature

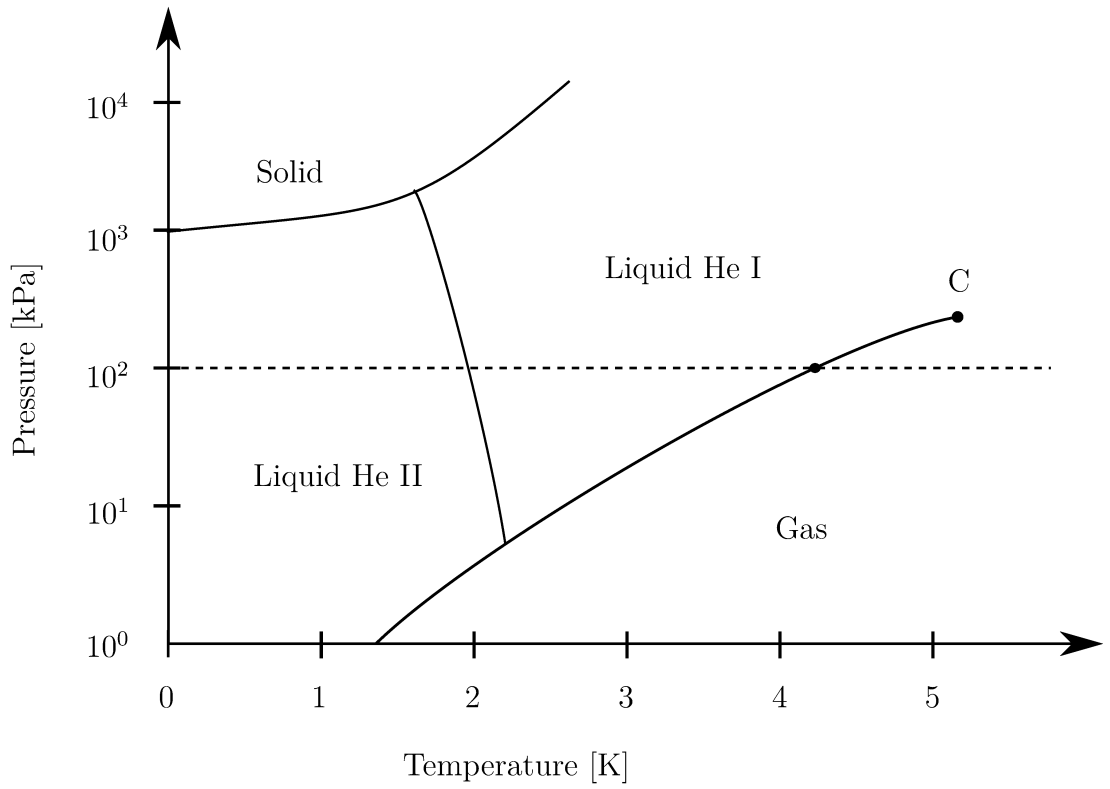

Figure 1.1: Equilibrium phase diagram for ^{4}He; the dashed horizontal line denotes the atmospheric pressure, C indicates the critical point.

dependence of the specific heat **c** peaks around this temperature [5]. Because of the shape of this dependence, the temperature is called T_λ and is equal to 2.17 K at saturated vapour pressure. The properties of ^{4}He differ above and below this temperature – the high temperature normal (viscous) phase and the low temperature superfluid phase. The two phases are known as helium I and helium II, respectively. ^{4}He undergoes a second order phase transition when we cross the lambda line.

Superfluidity

Above T_λ helium acts as a classical viscous liquid, described by the Navier-Stokes equation. However, below this temperature the description is not sufficient anymore and one needs some other theory to account for the behaviour of the fluid. We base our knowledge of the superfluid phase on several key experiments that aimed at measuring the fluid viscosity.

A way of measuring viscosity is performed in tubes and investigates the dependence of the exit velocity of the fluid at the end of the tube on the applied pressure. In 1939 this experiment was performed in He II [6], the flow rate was larger than

in classical viscous fluids and it was not proportional to the applied pressure – the flow rate was already large at the smallest applied pressure, saturated and then did not change when further pressure was applied.

Another option is to measure the drag force on a moving object, for example a torsional oscillator (a flat circular disc suspended vertically by an axial fibre). This is done by observing the damping of the oscillator. However when using this method, no damping was observed below T_λ [7].

Another experiment is the Andronikashvili's experiment, which was carried out in 1946 [8]. Instead of having one single disc, he used a whole stack of uniformly rotating discs. The measured quantity was the frequency of the rotation. He observed different behaviour above and below T_λ as for the previous experiments. When the applied force was the same, the oscillator frequency above this temperature was almost independent on temperature but below the frequency increased rapidly indicating the fall in the fluid viscosity.

These experiments showed that the behaviour of liquid helium cannot be described uniformly across the temperature range and that some properties of the liquid change with temperature significantly.

In 1930 another experiment, that contributed to the theory concerning liquid helium, showed that porous materials that do not allow regular liquids to flow through are not an obstacle for superfluid. Such so-called superleaks then inspired Allen and Jones [9], who 8 years later discovered **the fountain effect** (see fig. 1.2). A double walled test tube with fine powder is submerged into He II and the other side ends above the level. The powder allows the superfluid to go through easily. The flow can be generated just by heating. Hence by changing the temperature we generate the pressure difference. There is also an opposite effect – the mechano-caloric effect [10, 11].

The Two-Fluid Model

All of the experiments mentioned above led Landau and Tisza to develop their phenomenological model that described helium II as a mixture two fluids, one normal (viscous) and the second one superfluid (inviscid). The two components have their own velocity and density field, $\mathbf{v}_\mathrm{n}$ and ϱ_n for the normal fluid and $\mathbf{v}_\mathrm{s}$ and ϱ_s for the superfluid. Moreover, it is assumed that the normal fluid carries the entire entropy $\mathbf{s}$ of the system. The total density is the sum of the densities

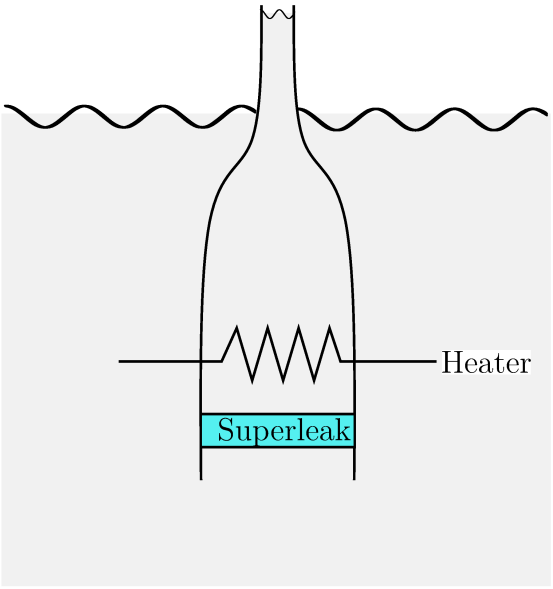

Figure 1.2: Illustration of the fountain effect; the superleak is made of a fine powder packed into a small cube, the heater causes changes in pressure, hence the difference between the levels.

of the two components, $\varrho = \varrho_{\mathrm{s}} + \varrho_{\mathrm{n}}$. The superfluid state is connected with the quantum ground state and the normal component consists of thermal excitations.

The individual densities are strongly dependent on temperature. However, the total density changes only slightly with temperature. From this we can say that the ratio of the two components changes with respect to temperature (see fig. 1.3)

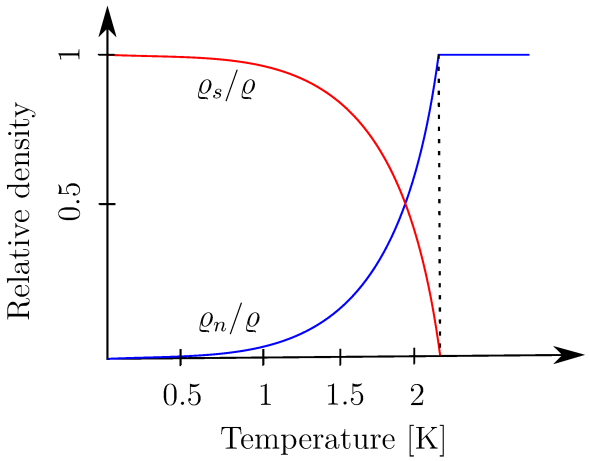

Figure 1.3: The temperature dependence of the relative normal and superfluid component densities.

By using this macroscopic model the unusual viscosity measurements can be sufficiently explained. Although the values of viscosities from the damping of the torsional oscillator and the flow through the tube experiments differ, they actually

support the two-fluid model. The tube method showed smaller values because it is determined by the superfluid flow. On the other hand, damping is caused by the more viscous component hence giving us larger values [7]. Andronikashvili's experiment further demonstrated the validity of the model. The increase of the oscillator frequency is an evidence of the changing proportion between the two fluids. The superfluid is not clamped to the discs, remains stationary in the surrounding vessel and does not contribute to the effective moment of inertia of the oscillator [12].

Types of Flows in Helium

The two fluid model is a macroscopic model and can be used to explain various types of flows [13]. The first one is called *coflow* and is generated mechanically, e.g. by moving objects. The normal and superfluid component move in the same direction, hence $\mathbf{v}_\mathrm{n} \approx \mathbf{v}_\mathrm{s}$. If we force the liquid through a porous material, the normal fluid component cannot pass due to its viscosity, on relevant time scales. As a result, behind such a wall (called superleak) there is a pure superfliud flow known as *superflow*.

The last one, called *counterflow*, is a consequence of the zero mass flux in closed channels. A (resistor) heater is placed at one end of the channel. It dissipates a know amount of heat flux $\dot{\mathrm{Q}}$ into the liquid. The heat is carried away by the normal component with a velocity $v_\mathrm{n} = = \dot{\mathrm{Q}}/(\varrho \mathrm{ST})$. This forces the superfluid component to move towards the heater with a velocity $v_\mathrm{s} = -(\varrho_\mathrm{n}/\varrho_\mathrm{s})v_\mathrm{n}$. We can then derive the counterflow velocity

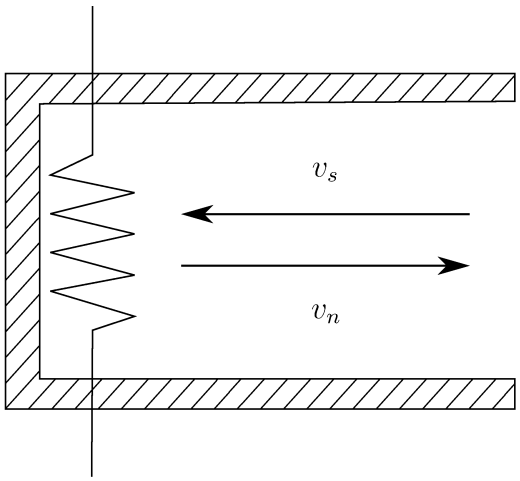

Figure 1.4: Schematic drawing of a He II thermal counterflow channel. The normal fluid carries the entropy away from the heat source, and because of the law of conservation of mass and momentum, the superfluid flows in the opposite direction.

$$v_\mathrm{ns} = v_\mathrm{n} - v_\mathrm{s} = \frac{\dot{\mathrm{Q}}}{\varrho_\mathrm{s}\mathrm{ST}} \tag{1.1}$$

Two-Fluid Model Equations

Mathematically this model can be described, often assuming the incompressibility of the liquid, $\nabla \cdot (\mathbf{v}_\mathrm{n} + \mathbf{v}_\mathrm{s}) = 0$, by the following equations for the momentum conservation of the normal fluid and superfluid components, respectively (derived for example in [1]).

$$\varrho_\mathrm{n} \left(\frac{\partial \mathbf{v}_\mathrm{n}}{\partial t} + (\mathbf{v}_\mathrm{n} \cdot \nabla)\mathbf{v}_\mathrm{n} \right) = -\frac{\varrho_\mathrm{n}}{\varrho} \nabla p - \frac{\varrho_\mathrm{s}\varrho_\mathrm{n}}{2\varrho} \nabla \left(\mathbf{v}_\mathrm{n} - \mathbf{v}_\mathrm{s} \right)^2 - \varrho_\mathrm{s} S \nabla T + \mathbf{F}_\mathrm{ns} + \eta \nabla^2 \mathbf{v}_\mathrm{n} \tag{1.2}$$

$$\varrho_\mathrm{s} \left(\frac{\partial \mathbf{v}_\mathrm{s}}{\partial t} + (\mathbf{v}_\mathrm{s} \cdot \nabla)\mathbf{v}_\mathrm{s} \right) = -\frac{\varrho_\mathrm{s}}{\varrho} \nabla p + \frac{\varrho_\mathrm{s}\varrho_\mathrm{n}}{2\varrho} \nabla \left(\mathbf{v}_\mathrm{n} - \mathbf{v}_\mathrm{s} \right)^2 + \varrho_\mathrm{s} S \nabla T - \mathbf{F}_\mathrm{ns} \tag{1.3}$$

In order to make further calculations feasible, we usually neglect some terms. Because of the large heat capacity we can say that $\nabla T \approx 0$, on average. We can disregard quadratic velocities as well as $\mathbf{F}_\mathrm{ns}$, the mutual friction force between the fluids (due to quantized vortices, see below). This gives us much simpler relations – the Euler equation for the superfluid and the Navier-Stokes equation for the normal fluid.

$$\varrho_\mathrm{s} \left(\frac{\partial \mathbf{v}_\mathrm{s}}{\partial t} + (\mathbf{v}_\mathrm{s} \cdot \nabla)\mathbf{v}_\mathrm{s} \right) = -\frac{\varrho_\mathrm{s}}{\varrho} \nabla p \tag{1.4}$$

$$\varrho_\mathrm{n} \left(\frac{\partial \mathbf{v}_\mathrm{n}}{\partial t} + (\mathbf{v}_\mathrm{n} \cdot \nabla)\mathbf{v}_\mathrm{n} \right) = -\frac{\varrho_\mathrm{n}}{\varrho} \nabla p + \eta \nabla^2 \mathbf{v}_\mathrm{n} \tag{1.5}$$

It is apparent that they are independent on each other, which results in two separate velocity fields. These last two equations are, however, not suitable for helium, because its components interact with each other, and, consequently, the mutual friction force is often kept in the equations to account for the coupling.

1.2 Quantum Behaviour

The roots of superfluidity nevertheless lie in its quantum behaviour. A volume of superfluid ^{4}He can be described by a single wave function

$$\Psi = Ce^{i\phi} \tag{1.6}$$

where the amplitude C and phase ϕ are functions of time and space. The macroscopic consequences are that the liquid parcel at one place is influenced by the ones at macroscopic distances away. From this description we can deduce the superfluid velocity $\mathbf{v}_\mathrm{s}$ to be

$$\mathbf{v}_\mathrm{s} = \frac{\hbar}{m_4}\nabla\phi \tag{1.7}$$

For simply connected volumes, this leads to potential flow with zero vorticity

$$\omega_\mathrm{s} = \nabla \times \mathbf{v}_\mathrm{s} = 0 \tag{1.8}$$

Quantized Vortices

However, it was shown from experiments in rotating helium [12] that the vorticity of the superfluid component can be non-zero. This was explained by Feynman and Onsager in their theory by assuming the existence of one-dimensional topological defects called quantized vortices. Their size is of the order of few ångstroms. In the core of the quantized vortex there is no longer any superfluid component left. They also divide the simply connected volume into multiply connected domains. The circulation Γ along closed curves is discrete and takes the value

$$\Gamma\left[\partial\Omega\right] = \oint_{\partial\Omega} \mathbf{v}_\mathrm{s} \cdot d\ell = 2\pi n \frac{\hbar}{m_4} = n\kappa \tag{1.9}$$

where n is a natural number and $\kappa = 9.97 \times 10^{-8}\,\mathrm{m}^2/\mathrm{s}$ [14] is the quantum of circulation.

Quantum Turbulence

For classical fluids equation 1.5 can be rewritten by using dimensionless variables, where the equation is scaled by the characteristic quantities of the flow, e.g. velocity U and length L, as follows

$$\frac{\partial v}{\partial t} + (v\nabla)\, v = -\nabla p + \frac{1}{Re}\nabla^2 v \tag{1.10}$$

where $Re = UL/\nu$ denotes the Reynolds number. From relation 1.10 we can conclude that flows with the same Reynolds numbers can be geometrically similar. The characteristics of the flow is dependent on the magnitude of the Reynolds number. If it is small, then we can neglect the nonlinear term $(v\nabla)\, v$ and the viscosity is the dominant term and we observe laminar flows. If, on the other hand, Re is large, the viscosity is disregarded and the nonlinear term may lead to instability in the flow and hence turbulence occurs.

For He II counterflow we can also define a Reynolds number [15], e.g., as

$$Re = \frac{\varrho v_{vs} D}{\mu} \tag{1.11}$$

where D is the relevant length scale and μ denotes the dynamic viscosity of the normal component of He II. Laminar flows, which means, e.g. parallel configuration of quantized vortices, can be found for example in rotating baths as the vortices tend to align in a vortex lattice. In counterflow the liquid can experience a turbulent arrangement if a critical critical heat flux $\dot{\mathrm{Q}}_{\mathrm{c}}$ is exceeded. The measured quantity, for $\mathbf{v}_{\mathrm{ns}}$ large enough, is the vortex line density [16]

$$L = \gamma^2 {\mathbf{v}_{\mathrm{ns}}}^2 \tag{1.12}$$

where γ [17] is temperature-dependent parameter.

The mean distance between vortices is called the quantum length scale s_q [18]

$$s_q = \frac{1}{\sqrt{L}} = \frac{1}{\gamma v_{ns}} \tag{1.13}$$

From the quantum length scale we can find a corresponding quantum time, the

time needed to travel the distance s_q with the velocity V, as

$$t_q = \frac{s_q}{V} = \frac{1}{V\gamma v_{ns}} \tag{1.14}$$

These relations will prove to be important parameters for our studied case of counterflow turbulence in the proximity of the heater – the boundary perpendicular to the main flow.

2 Experimental Techniques

In the following section we present techniques used in low temperature flow visualization, as well as the set-up of the experiment itself.

2.1 Flow Visualization

Various experimental methods, such as measuring the temperature difference and the second sound attenuation by quantized vortices, have been used over the years to study flows of He II, for example, to obtain information on the average vortex line density in the experimental volume. Here, we employ another approach, which, as shown below, also gives us useful physical insight, that is, flow visualization.

The first experiment aiming to visualize superfluid flows were performed in 1957 by Chopra [19]. In the following years, this field did not receive much attention. It was then brought back at the forefront by the work of Zhang and Van Sciver [20], see also the recent review [21].

Particle Tracking Velocimetry and Particle Image Velocimetry

In classical fluid dynamics, Particle Tracking Velocimetry (PTV) is a commonly used technique [22]. It has shown to be a more accurate method when working with quantum flows than Particle Image Velocimetry (PIV) because of the two velocity fields in counterflow, when it is unclear whether the obtained velocities represent those of the normal component, the superfluid component or a mixture of the two. The method is based on particles following the motion of the liquid. Particles are injected into the fluid and illuminated with a laser sheet. A high-frequency camera then captures their position in time. This allows to investigate

the velocity of the particles from their displacement. PIV is instead an Eulerian method describing the instantaneous velocity field. On the other hand PTV takes the Lagrangian approach and tracks individual particles and their trajectories in time [23].

2.2 Solid Particles

There are several criteria that particles have to meet in order to be suitable for cryogenic experiments. Their size should be such that their presence does not affect significantly the flow but only probe it. They also should be neutrally buoyant so that they do not settle down or float and faithfully follow the flow fields. Finding neutrally buoyant particles is very challenging, the density of Helium II being $\varrho = 145.5 \pm 0.4\,\mathrm{kg/m^3}$ [14]. In previous works, deuterium particles showed to be suitable for these types of experiments. Their density $\varrho_{D_2} = 200\,\mathrm{kg/m^3}$ is slightly larger than that one of helium [24].

Seeding System

As mentioned above, suitable particles are vital when it comes to PTV. Deuterium particles were used in the experiment discussed here.

If we were to inject the deuterium directly into liquid helium, the gas would solidify into particles of various sizes. Therefore deuterium is firstly mixed with helium at room temperature. It has been experimentally tested, that the ideal size of particles is when the ratio between deuterium and helium is about 1:100. This mixture is then injected into the cryogenic helium. Then deuterium solidifies into small particles and helium either liquefies or boils away.

2.3 Experimental Setup

The experiment was performed in Prague by using the low temperature visualization setup of the Department of Low Temperature Physics. The experiment is shown schematically in fig 2.3. It contains a custom-made cryostat with optical access, laser, and high-frequency camera.

Cryostat

The cryostat is an apparatus that is used to reach and maintain very low temperatures. As the temperature in the experiment is around 1.5 K, an evaporation cryostat was used (see fig. 2.1).

In order to prepare the experiment, the cryostat is firstly pre-cooled with liquid nitrogen, at ca. 77 K. Then it is filled with liquid helium to reach temperatures around 4 K. Then adequate pumps start to pump off the vapours to cool the cryostat even further.

The cryostat's inner volume is usually filled with up to 60 l of liquid helium. There are two types of insulation used – liquid nitrogen bath and vacuum space.

The liquid nitrogen vessel contains 35 l of the cryogenic liquid. It acts as a shield from the outside radiation, which could cause unwanted heat transfer to the experimental volume. It is also used to pre-cool the cryostat before it is filled with helium.

Another obstacle for reaching low temperatures can be simply heat conductivity. To prevent this from happening, the inner volume as well as the nitrogen container are surrounded by vacuum vessels. The pressure inside is of the order of 1 mPa

For the purpose of the PTV technique, optical access to the experimental volume has to be ensured. For that reason there are 5 identical circular optical ports of 25 mm diameter at the bottom of the cryostat – one from each side and one from the bottom. Each optical port has 2 quartz and one sapphire windows.

Experimental Channel and Visualization Apparatus

The windows at the bottom of the cryostat allow optical access to the experimental channel (dimensions $50 \times 50 \times 300$ mm). On the vertical axis of the insert the cell is attached (see fig. 2.2). The cell has a square cross-section, and at the bottom a heater is placed (its dimensions are the same as those of the cell). In this experiment the area of concern was the proximity of this heater so the windows were aligned with the bottom of the cell. At the top of the cell a small tube is attached. It is used to prepare the particles as well as to further mix the helium (and particles) during the experiment.

Outside the cryostat a high-frequency camera captured the particle motion with

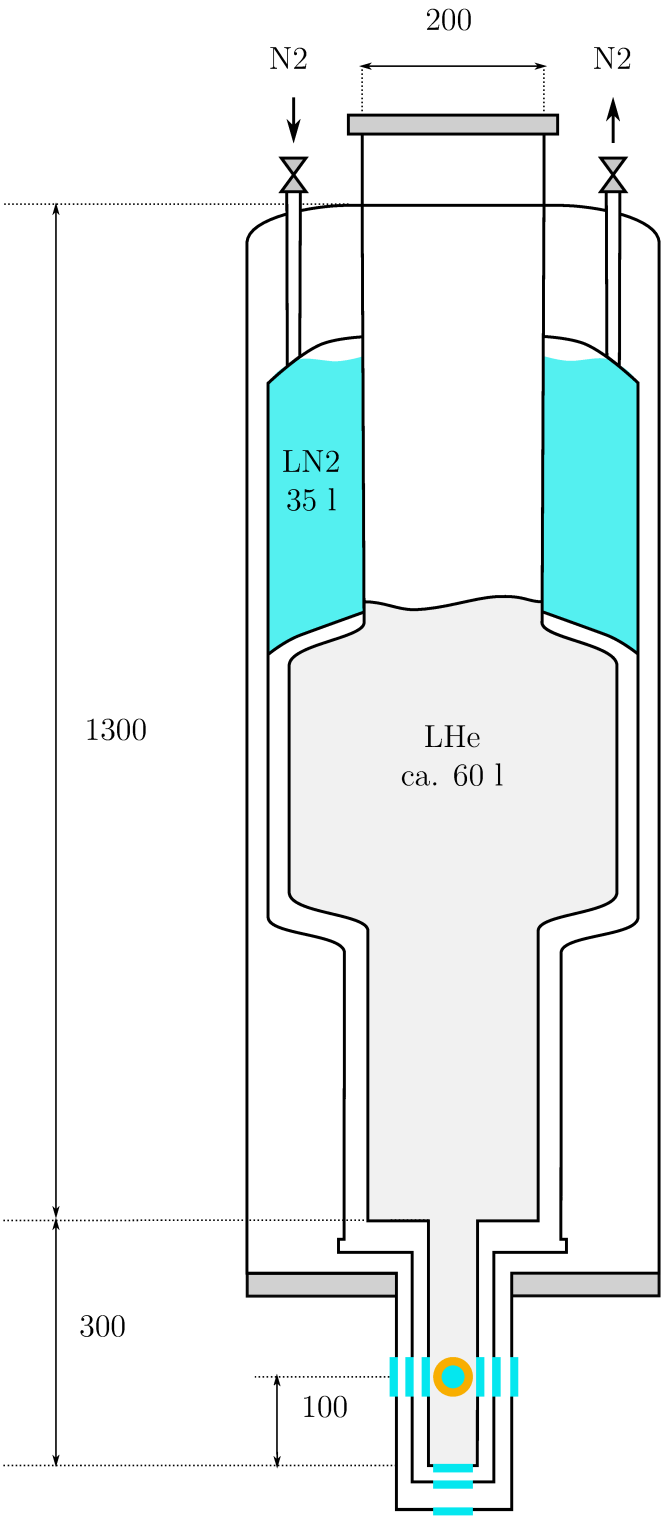

Figure 2.1: Simplified scheme of the cryostat. The inner vessel is for liquid helium and during the experiments reaches temperatures below 4 K, inside this vessel there is the insert on which the cell is mounted. The outer vessel containing liquid nitrogen is used as thermal insulation. The space between the vessels and the outer wall is pumped to medium vacuum (ca. 1 mPa) for thermal insulation. At the very bottom there are 5 optical ports to the cryostat (windows are in light blue). All dimensions are in millimetres.

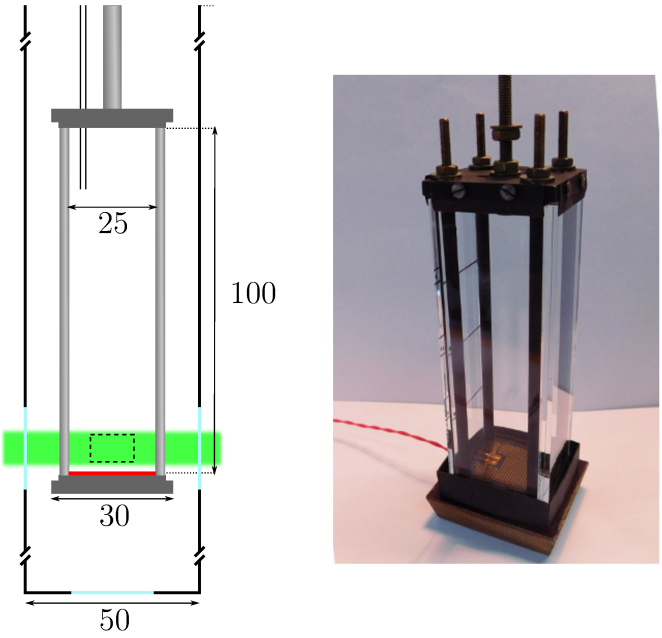

Figure 2.2: Left: Scheme of the counterflow cell with the field of view (green rectangle). The red rectangle represents the planar heater. When it is turned on, the flow is generated in the cell perpendicularly to the heater. The flow is observed via glass windows (light blue) and visualized by the particles that are injected into the volume through a tube connected to the top of the cell. All dimensions are in millimetres. Right: photo of the cell.

rates of 500 fps. The laser illuminated a plane perpendicular to the camera field of view and provided enough light for the pictures while not supplying noticeable amount of heat – ca. 0.1 W [23].

2.4 Data Acquisition

Throughout the duration of the experiment, the amount of heat supplied to the heater and the temperature was constantly recorded so that the exact conditions of the experiment can be taken in consideration during further processing. To obtain the pictures we used a camera that captured 1 Mpx bitmap image sequences, one pixel corresponding to 10 μm. Each sequence had around 2000 images. Usually we collected several sequences for every temperature and heat flux in order to have enough data for further processing. The frame rate has to be high enough to ensure that the positions are connected correctly, that the trajectories are not mixed up, and to capture the fine details of the structure of the flow.

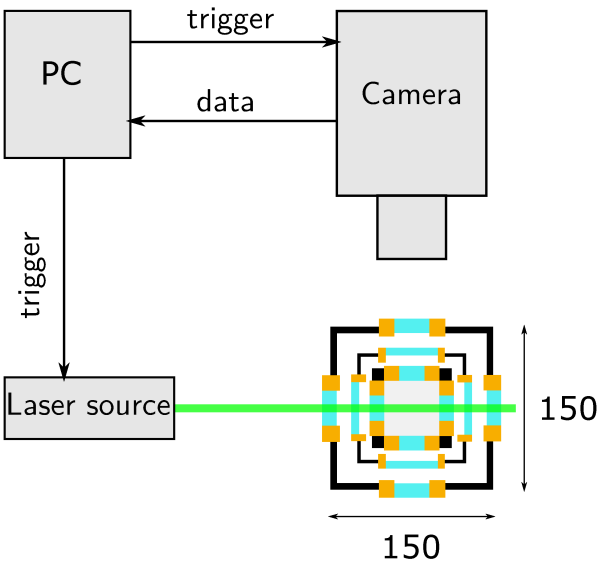

Figure 2.3: Scheme of the visualization setup and its communication with PC (top view). At the right bottom there is the tail of the cryostat containing optical access through windows (light blue, window supports are brown).The tail is of square cross section of 50 mm sides and 300 mm high. The laser plane, used for visualization, is depicted as a green line. Perpendicular to it there is a camera focused into the laser plane. The dimensions are given in millimetres.

Image Processing

The output data were pictures which needed further processing in order to extract the information. In order to extract the information from the image, we have to detect the particles. This is done by using the open-source software ImageJ with a subroutine called Mosaic [25, 26]. Firstly, the brightness of the picture has to be corrected for optimal detection of particles. Mosaic is then run. It detects groups of pixels that are brighter than the surrounding in each picture and saves the position in terms of pixel positions. When particles in all the images are detected, it then links the positions together to form the trajectories.

Since only a thin plane is illuminated, particles can seemingly disappear from the view which results in short tracks. To avoid this, there is a possibility to connect two trajectories together even if there is one or two points missing. However, the software can sometimes connect two different tracks together so these connected points have to be checked.

Velocity Estimation

The data handling has great influence as it can bring systematic error into the results. Since the data, positions, obtained experimentally are determined with some uncertainty due to the camera resolution, the resulting velocity data, will be uncertain as well. The extent of such error is also dependent on the calculation method [27]. There are countless ways how to estimate the velocity form given position in time. These methods then influence the outcome of the whole experiment.

I compared different methods of derivations. The first one was linear numerical derivation which used two adjacent points. The results were quite noisy as it did not apply any smoothing to the raw data. One can also use higher polynomials to fit the track and then perform the derivative.

In order to determine the most suitable fit and number of trajectory points taken into account for each fit, the velocity standard deviation was used. As the calculation of the derivative takes into account more distant points, we should see the decrease in standard deviation and from some point reach a plateau. This means that the change of the parameter, in this case the number of points, does not influence the results.

The results showed that linear and quadratic functions work nicely, while for the cubic polynomial the parameters have to be check for each data set as the constant evolution of the standard deviation was not observed. The higher the polynomials, the more untruthful the fit may be, as some artificial peaks may occur due to more degrees of freedom. If one's data have a lot of noise, useful fitting is done by convolution with Gaussian kernel [27]. In this experiment, we used the linear method and then smoothed linearly the velocities using different filter in a dedicated programme called Statistika.

3 Results and Discussion

Our aim was to compare the behaviour of thermal counterflow close to the heater as oppose to the one in the bulk. The data obtained from the measurements were processed as explained previously. The temperatures ranged from 1.24 K to 2.10 K with various values of heat flux (see table 3.2). The bulk data, used for comparison, were taken from previous experiments with deuterium and hydrogen particles [28].

As stated previously, flows can be classified based on their Reynolds numbers. The hydraulic diameter of our channel, the relevant length scale in equation 1.11, is $D = 25\,mm$. The dynamic viscosity [14] is listed in table 3.1, which gives Reynolds numbers $Re \geq 4000$. In [29] the transition to turbulent flow has been estimated for this particular channel and it corresponds to $Re \approx 2300$. Hence, we can say that our flows are turbulent.

The diffusion time t_d can be said to be the time needed for the heat to diffuse through a certain volume from the heated region. Therefore it is an indicator if we reach the steady state or if we are observing unsteady flow. We find that this time is several orders of magnitude smaller than the time elapsed before collecting the movies. Hence, it is possible to say that the steady state has been reached and that the comparison with the bulk counterflow is justified [3].

$T[K]$	$\nu[10^{-6}Pa \cdot s]$	$\varrho[kg/m^3]$	$\gamma[s/cm^2]$
1.95	1.4	146	110
1.94	1.4	146	205
1.77	1.3	145	210
1.75	1.3	145	280
1.40	1.5	145	285
1.24	1.9	145	345

Table 3.1: Tabulated dynamic viscosity ν, density ϱ [14] and γ [17] for relevant temperatures.

	$T[K]$	$q[W/m2]$	$v_{ns}[mm/s]$	Re
$D1$	1.24	23	2.2	4000
$D2$	1.40	54	2.2	5200
$D3$	1.75	235	2.7	7600
$D4$	1.95	234	1.9	5000
BH	1.77	612	6.8	19000
BD	1.77	608	6.8	18800

Table 3.2: Experimental conditions, such as temperature, heat flux, counterflow velocity 1.1, Reynolds numbers 1.11, for runs with deuterium particles D1–D4, the second number represents cases with different temperature and heat flux; BH and BD represents bulk data from previous experiments.

3.1 Probed Scales

In the theoretical chapter we introduced the quantum length scale s_q (eq. 1.13). This is not, however, the scale that we can access experimentally due to the finite particle size. Hence in an ideal case the minimal observable scale is the one that corresponds to the size of the particles which is of the order of few microns. Their size can be estimated from their settling velocity as shown in [24]. This particle scale s_p is also dependent on the frame rate, i.e. on the distance between two consecutive position we captured. Therefore we estimate it from the mean velocity V of particles and the time. This leads to $s_p = Vt$. We can obtain information about larger flow scales by removing positions from tracks and so prolong the time difference between two positions and calculate new corresponding velocities. Note that the mean velocity is calculated from the highest frame rate, so it does not change with the transition towards larger flow scales. The highest frame rate determines the minimal time between two positions we can access, for the case of our measurements this gives us $t_{min} = 0.2\,\mathrm{ms}$. We can associate these scales with their ratio, which can be also rewritten in terms of time [30]

$$R = \frac{s_p}{s_q} = \gamma v_{ns} V t \tag{3.1}$$

When we consider large-scale flows we can see the gradual disappearance of quantum effects and transition to classical-like behaviour. For classical fluids and for flows probed at large scales the velocity distribution is close to Gaussian [31]. For the case of He II, this should happen for $R \geq 1$. The transition is apparent at ve-

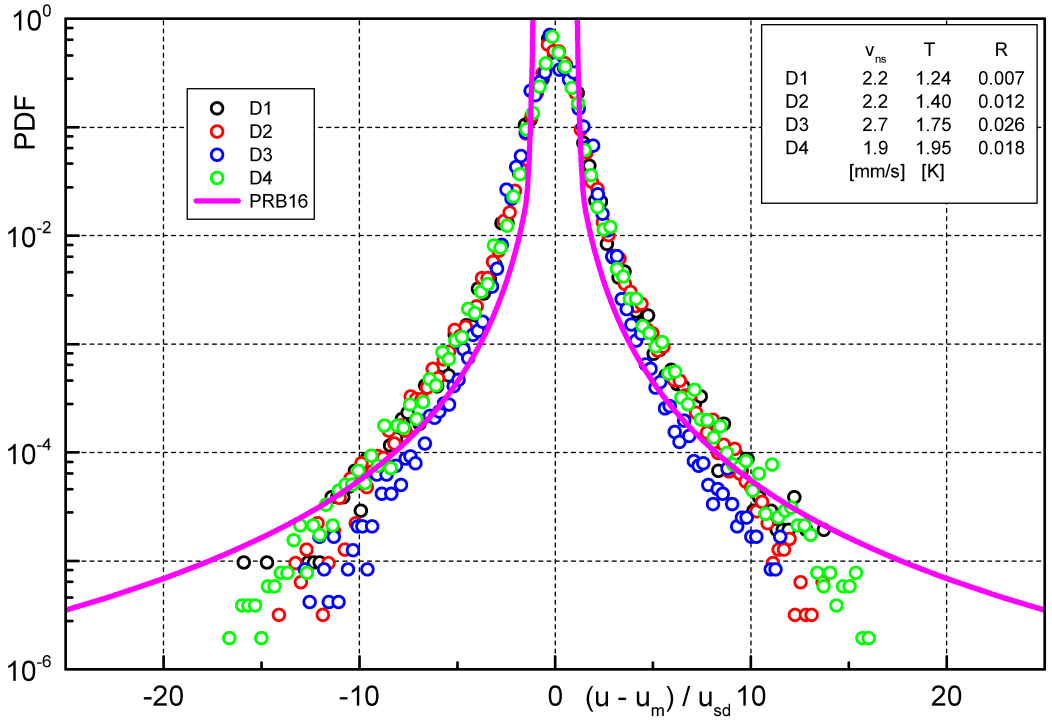

Figure 3.1: PDF of the horizontal velocity obtained in the heater proximity – cases with deuterium particles D1–D4, the fit is in accordance with [30] $C/\left|(u-\bar{u})/u^{sd}\right|$ and it is labelled in the figure as PRB16.

locity distribution as the distribution looses its tails and becomes Gaussian-like. This assumption was confirmed for the behaviour of He II in the bulk [30].

3.2 Velocity Distributions

A typical depiction of the probed flow is by using Probability density functions (PDF) of the normalized particle velocity $(u-\bar{u})/u^{sd}$, where u is the velocity component in the horizontal direction, $\bar{u}$ the mean velocity, and u^{sd} the standard deviation. The same procedure is used also for the vertical component v. The way we obtained our data allowed us only to learn about the velocity in two dimensions. This, however, should not be a problem as thermal counterflow can be sufficiently described by a planar velocity perpendicular to the flow source. For the bulk data the PDF has a quasi-Gaussian core with power-law tails, which follow $P(v) \propto v^{-3}$ [30]. The transition to Gaussian distribution happens when we increase the time step and we can see the gradual disappearance of the tails towards the Gaussian parabola (in semilog plot). We can see that data obtained close to the heater do not follow the v^{-3} tail distribution unlike the bulk data.

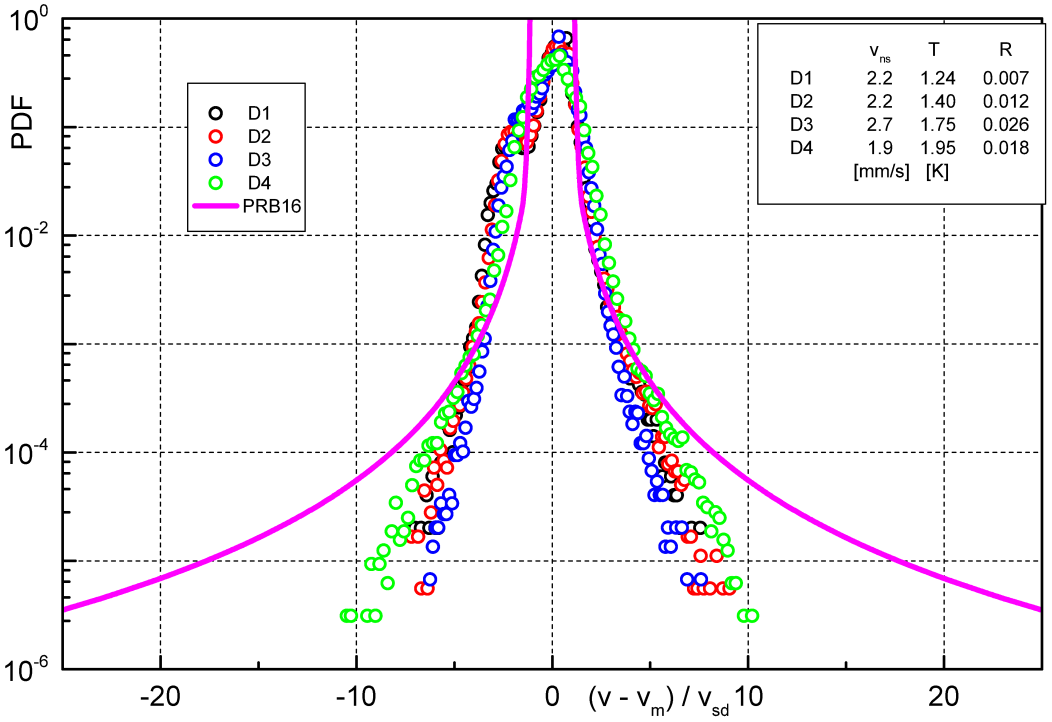

Figure 3.2: PDF of the vertical velocity obtained in the heater proximity – cases with deuterium particles D1–D4, the fit is in accordance with [30] $C/\left|(v-\bar{v})/v^{sd}\right|$ and it is labelled in the figure as PRB16, the two peaks are consequences of the counterflow.

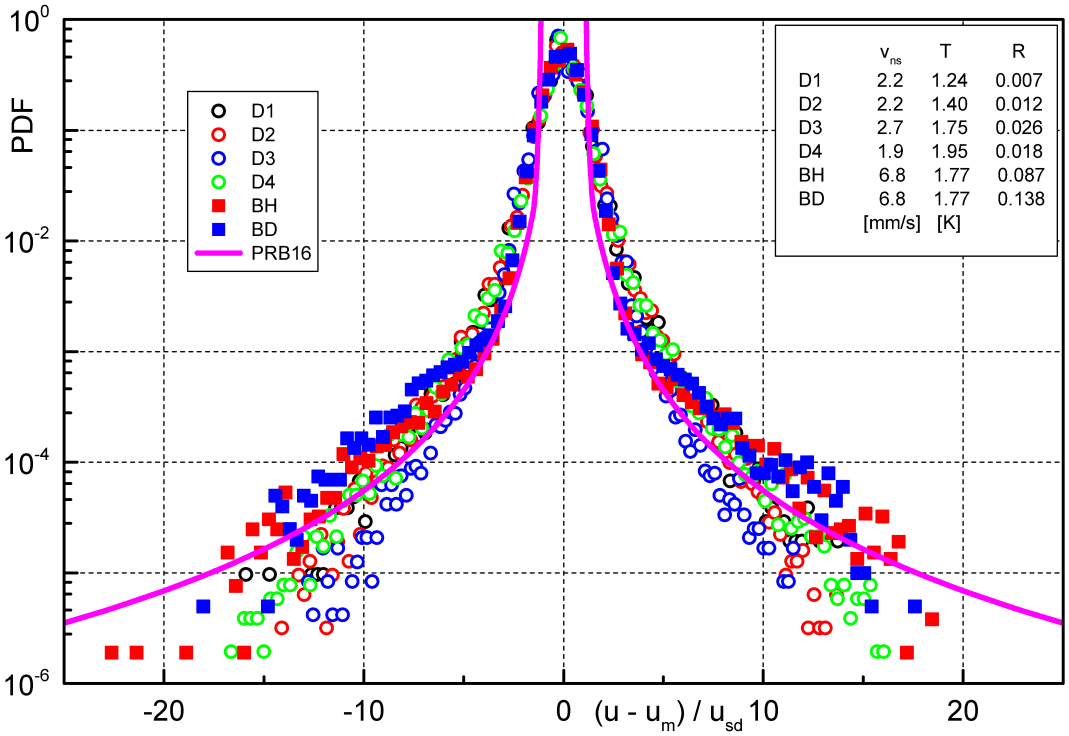

Figure 3.3: PDF of the horizontal velocity obtained in the heater proximity – cases with deuterium particles D1–D4; BH and BD are bulk data from previous experiments, for hydrogen and deuterium particles, respectively.

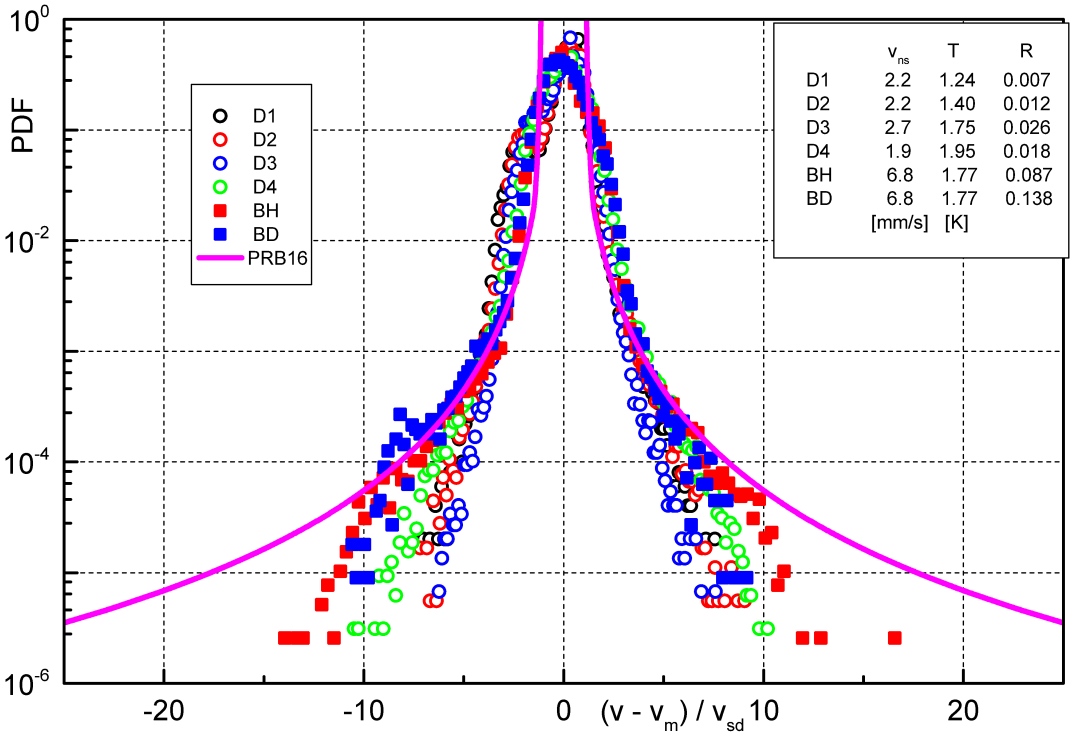

Figure 3.4: PDF of the vertical velocity obtained in the heater proximity – cases with deuterium particles D1–D4; BH and BD are bulk data from previous experiments, for hydrogen and deuterium particles, respectively.

Note that for the vertical velocity the distribution has two broad peaks. This is a typical shape for counterflow. The bigger one can be attributed to the normal component as it drags the particles more than the vortices in the superfluid component. Therefore the peaks have different signs and they should be more pronounced for lower values of v_{ns}.

From figure 3.3 we can conclude that the data, obtained in the proximity of the heater do not follow the power-law velocity distribution unlike the bulk data. However, their distribution is not fully Gaussian either. Following the previous reasoning about the transition from quantum to classical-like flows, this distribution is somewhere in between the two, hence, in the transition to larger scale flows. If we calculate the fourth momentum, i.e. the flatness, of the Gaussian distribution, we find it to be 3. We decided to check the difference between our velocity distribution and Gaussian distribution with the value of the flatness (see fig. 3.5). We know we reached the Gaussian-like distribution, when the flatness is 3. We plotted the dependence of the flatness on the scale ratio R. For the bulk data published previously, the distribution becomes Gaussian at the expected value of $R \approx 1$. As a result, for values $R \leq 1$ the velocity distribution is ruled by the power-law tails at small scales.

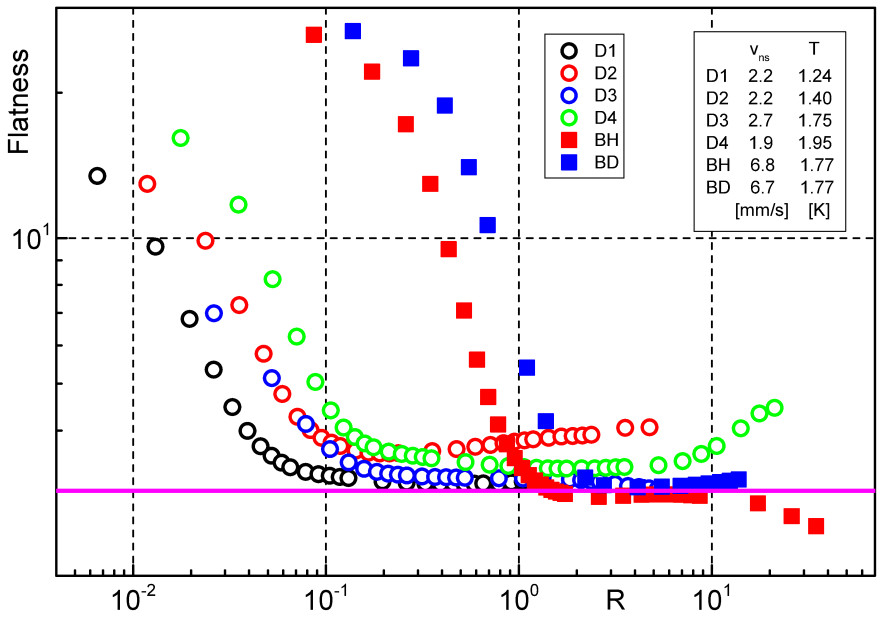

Figure 3.5: Flatness of the horizontal velocity distribution calculated for various values of R, magenta line is the flatness of the Gaussian distribution.

This is not however the case for the data obtained close to the heater. The drop down to flatness equal to 3 occurs for the R about one order of magnitude smaller than for the bulk case. As the scales probed by the particles remain presumably the same, the change had to be in the quantum scale. This means that quantized vortices are roughly 10 times closer to each other than in the case of the bulk. In other words, the tangle seems to be much denser in the heater proximity in otherwise similar conditions.

In order to be able to compare the results and the shift in quantum length scale, we introduced an effective scale ratio R_1. The relation to the previous ratio R is the following

$$R_1 = cR = c\gamma v_{ns} V t \tag{3.2}$$

The parameter c, which scales the effective scale ratio, indicates how denser the vortex tangle is, i.e. vorticity enhancement. We shown the flatness in relation to the effective scale ratio in figure 3.6. Corresponding values of the scaling parameter c are listed in table 3.3.

From previous estimations and experiments it is also possible to compare the behaviour of hydrogen and deuterium particles [28]. When particles are moving in the flow, there is a significant influence of inertia that determines how similar

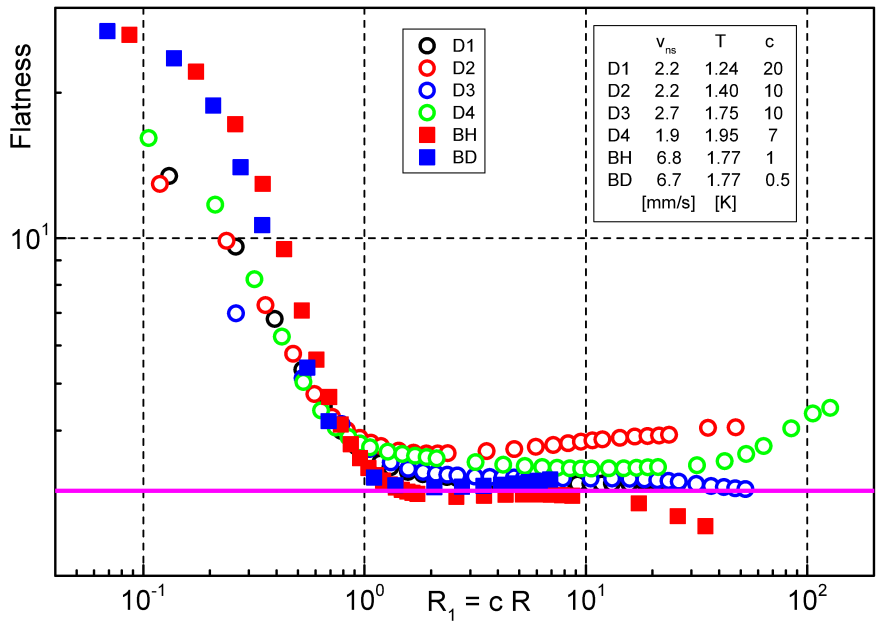

Figure 3.6: Flatness of the horizontal velocity distribution calculated for various values of R_1 (R scaled by the parameter c), magenta line is the flatness of the Gaussian distribution.

	$v_{abs}[mm/s]$	v_{abs}/v_{ns}	$s_p[\mu m]$	$s_q[\mu m]$	$t_q[ms]$	$c(R1)$
$D1$	2.2	1.0	4.4	413	187	20
$D2$	2.4	1.1	4.9	371	153	10
$D3$	2.3	0.9	4.7	232	100	10
$D4$	1.6	0.8	3.2	272	169	7
BH	2.4	0.4	4.8	92	38	1
BD	3.9	0.6	7.7	92	24	0.5

Table 3.3: Linearly calculated velocities and scales for all experimental run as well as values of c used to calculate the effective scale ratio.

the particle trajectories are compared to the flow movement. This is related to added mass, which describes the inertia added to the system because of the fluid volume that moves with an accelerating or decelerating body. If the densities are the same, then the particles tend to accelerate with the same rate as the fluid. When there is inequality of the densities, we observe the particle acceleration to be faster, for the case of $\varrho_f > \varrho_p$, or slower than the fluid, when $\varrho_f < \varrho_p$. This can be expressed by the coefficient $K_p = \frac{1+C}{\varrho_p/\varrho_f+C}$, where ϱ_f and ϱ_p are the fluid and particle densities and C is the added mass coefficient. For spherical particles the added mass coefficient is $C = 1/2$, which gives us $K_H/K_D \approx 1.7$ in He II. Hydrogen particles hence should accelerate roughly two times faster than deuterium particles. This can be seen also from our data as the corresponding

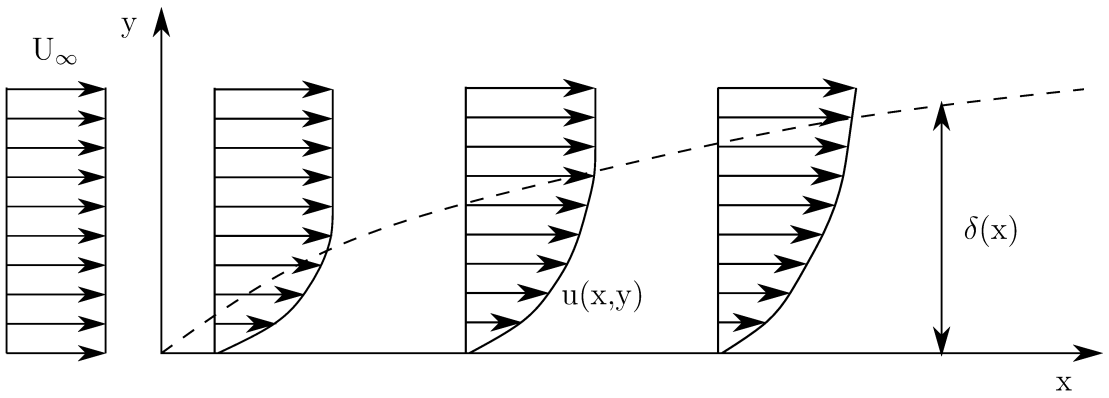

Figure 3.7: Boundary layer thickness δ in the tube depends on the distance from the entrance (at $x = 0$), y axis is pointing towards the center of the tube, $u(x, y)$ is the velocity of the flow in space, U_∞ is the free flow velocity, unaffected by the presence of the boundary.

effective ratio has coefficient $c = 0.5$ for deuterium particles.

There is also the phenomenon of the parameter c decrease in response to increasing temperature. The only other quantity, that is temperature dependent in the definition of R_1 (eq. 3.2), is γ which is increasing with temperature. This could therefore mean that c has to compensate for this increase so that R_1 remains constant.

As comprehensive theoretical models have yet to be developed, experimental examination gives useful insight into the problem and in the following we propose a number of physical explanations.

We can start by considering the wall-bounded superfluid flow investigated numerically in [32]. The assumptions for the superfluid behaviour close to the boundary are that there is a slip in the velocity component tangential to the surface and that the component perpendicular to the boundary is null. They concluded that the roughness of the surface, comparable to the vortex core size, may generate new vortices. Although their area of interest was only few microns from the boundary, their results can be applied in our case as some of the vortices are then ejected into the bulk in the form of vortex rings (in the shape of closed loops).

For viscous fluids, on the other hand, there exists a region, called boundary layer, where the friction between a moving fluid and the wall plays a significant role and affects the velocity field. Its thickness for laminar flows can be expressed by

the Blasius equation as [33]

$$\delta \sim \sqrt{\frac{\nu x}{U_\infty}}, \tag{3.3}$$

where ν is the kinematic viscosity, x the distance from the channel entrance, and U_∞ is velocity of the outer flow (for a graphical depiction see fig. 3.7). The Blasius equation does not describe flows with the same conditions as in this experiment, however, we can use it as an upper limit of the thickness for the boundary layer, since this region is thinner in turbulent flows [33].

In order to understand the observed enhancement we must come up with an explanation that unifies these two very different cases. We can notice that the counterflow velocity is a macroscopic feature (see eq. 1.1) and hence does not anyhow take into account the geometrical position of the field of view. The relation between the counterflow velocity and the vortex line density (eq. 1.12) thus implies that the gamma values depend on the position of the studied region. Therefore, as the literature values of γ [17] were obtained in the bulk, this equation holds only for bulk measurements. This could also explain the differences in the γ values from other experiments (e.g. [34]) as they were obtained at different distance from the boundaries (we introduced parameter c in order to compensate for this property.)

The denser vortex tangle can be attributed partially to the roughness of the top of the heater. On scales relevant to quantized vortices, almost every material surface has a noticeable texture. Because of this the flow induced by the heater generates vortices not only by stretching already existing vortices but also by offering pinning spots for the new ones [32].

A similar behaviour can be seen in counterflows near walls parallel to the flow. As pointed out in [35], the vortex line density increases close to the boundary. The explanation for this was attributed to the velocity of the normal component, which is larger in the bulk than close to the wall due to the friction between the wall and the fluid. The velocity of the viscous fluid therefore is a local feature depending on the distance from the boundaries (e.g. walls, heater) and the largest it is, the more vortices stretch out and are pushed to the boundary regions.

As mentioned previously, classical boundary layer theory predicts different boundary layer thickness depending on the distance from the channel entrance (see figure 3.7 and equation 3.3). Our assumption is that the boundary layer closer to

the heater on the vertical walls is thinner than further down the flow. In the case of a closed channel with the heater producing the counterflow the vortices can also be pushed to the boundary where the velocity is smaller than in the bulk.

Moreover, the vortices are carried by the superfluid component which is moving towards the heater (see figure 1.4). Because of this, the vortices may accumulate in the bottom region of the channel and thus generate a denser tangle.

4 Conclusions

A series of experiments concerning thermal counterflow of liquid helium was carried out. We investigated, for the first time by visualization, the flow region close to the heater, the flow source. For various conditions, we captured the movements of deuterium particles suspended in the liquid and computed their velocities.

For the velocity distributions obtained in the heater proximity, the behaviour of the bulk data with distinct power-law tails – of quantum origin – was not observed at the smallest scales probed by the particles. It is, however, apparent from the dependence of the distribution flatness on the scale ratio, see equation 3.1, that the vortices are significantly closer to each other in the heater proximity than in the bulk, at least in the range of investigated parameters.

In order to compare the data taken in different flow regions, we introduced the parameter c, see equation 3.2, which scales the distribution flatness. We found corresponding values to be up to 20 times larger close to the heater than in the bulk. Therefore, we argue that a significant vorticity enhancement occurs in the heater proximity.

We suggested that a physical explanation might be the roughness of the surface, where nucleation as well as pinning points for the vortices may exist [32]. Another reason might be related to the velocity of the normal component which is expected to be larger in the bulk, due to the friction between the wall and the fluid, and hence the fluid might be pushing the vortices closer to the boundary regions [35].

The results of this experiments were published in Physical Review B [3]. Future experiments may try to investigate more closely the thickness of relevant boundary layers. The channel geometrical properties may also influence the observed enhancement of the vortex line density. Such studies could lead to deeper understanding of turbulence not only in superfluids but also in viscous fluids.

Bibliography

[1] L. Skrbek et al. *Fyzika Nízkých Teplot*. MatfyzPress, 2011.

[2] L. Landau. Theory of the superfluidity of helium II. *Physical Review*, 60(4):356–358, 1941.

[3] P. Hrubcová, P. Švančara, and M. La Mantia. Vorticity enhancement in thermal counterflow of superfluid helium. *Phys. Rev. B*, 97(6):064512, 2018.

[4] H. Kamerlingh O. *The liquefaction of helium.*, pages 164–187. Springer Netherlands, Dordrecht, 1991.

[5] L. I. Dana and H. K. Onnes. *Further experiments with liquid helium. BB. Preliminary determinations of the specific heat of liquid helium*, pages 227–235. Springer Netherlands, Dordrecht, 1991.

[6] J. F. Allen and A. D. Misener. The properties of flow of liquid He II. *Proceedings of the Royal Society A*, 172:467–491, 1939.

[7] T. Guénault. *Basic Superfluids*. Master's Series in Physics and Astronomy. CRC Press, 2003.

[8] E. L. Andronikashvili. A direct observation of two kinds of motion in Helium II. In Z. M. Galasiewicz, editor, *Helium 4*, pages 154 – 165. Pergamon, 1971.

[9] J. F. Allen and H. Jones. New phenomena connected with heat flow in Helium II. *Nature*, 141:243–244, 1938.

[10] J. G. Daunt and K. Mendelssohn. The transfer effect in liquid He II. I. the transfer phenomena. *Proceedings of the Royal Society A*, 170:423–439, 1939.

[11] J. G. Daunt and K. Mendelssohn. The transfer effect in liquid He II. II. properties of the transfer film. *Proceedings of the Royal Society A*, 170:439–450, 1939.

[12] E. L. Andronikashvili and Y. U. G. Mamaladze. Quantization of macroscopic motions and hydrodynamics of rotating Helium II. *Reviews of Modern Physics*, 38(4):567–625, 1967.

[13] C. F. Barenghi and Y. A. Sergeev. *Vortices and Turbulence at Very Low Temperatures*. Springer, 2008.

[14] R. J. Donnelly and C. F. Barenghi. The observed properties of liquid helium at the saturated vapor pressure. *Journal of Physical and Chemical Reference Data*, 27:1217–1274, 1998.

[15] T. Xu and S. W. Van Sciver. Particle image velocimetry measurements of the velocity profile in He I forced flow. *Physics of Fluids*, 19(7):071703, 2007.

[16] E. Varga, S. Babuin, and L. Skrbek. Second-sound studies of coflow and counterflow of superfluid ^{4}He in channels. *Physics of Fluids*, 27:065101, 2015.

[17] Y. A. Sergeev, C. F. Barenghi, and D. Kivotides. Motion of micron-size particles in turbulent helium II. *Physical Review B*, 74(18):184506, 2006.

[18] M. La Mantia and L. Skrbek. Quantum, or classical turbulence? *EPL (Europhysics Letters)*, 105(4):46002, 2014.

[19] K. L. Chopra and J. B. Brown. Suspension of particles in liquid helium. *Physical Review*, 108(1):157–157, 1957.

[20] Tao Zhang and Steven W. Van Sciver. Large-scale turbulent flow around a cylinder in counterflow superfluid ^{4}He (He (II)). *Nature Physics*, 1:36–38, 2005.

[21] W. Guo, M. La Mantia, D. P. Lathrop, and S. W. Van Sciver. Visualization of two-fluid flows of superfluid helium-4. *Proceedings of the National Academy of Sciences*, 111(Supplement 1):4653–4658, 2014.

[22] M. Raffel, Ch. E. Willert, J. Kompenhans, et al. *Particle image velocimetry: a practical guide*. Springer Science & Business Media, 2007.

[23] D. Duda, M. La Mantia, M. Rotter, and L. Skrbek. On the visualization of thermal counterflow of he ii past a circular cylinder. *Journal of Low Temperature Physics*, 175:331–338, 2014.

[24] M. La Mantia, T. V. Chagovets, M. Rotter, and L. Skrbek. Testing the performance of a cryogenic visualization system on thermal counterflow by using hydrogen and deuterium solid tracers. *Review of Scientific Instruments*, 83(5):055109, 2012.

[25] MOSAIC group. ImageJ Particle Tracker. `https://imagej.net/Particle_Tracker`. Accessed: 2018-06-22.

[26] I. F. Sbalzarini and P. Koumoutsakos. Feature point tracking and trajectory analysis for video imaging in cell biology. *Journal of Structural Biology*, 151(2):182–195, 2005.

[27] P. Švančara, P. Hrubcová, and M. La Mantia. Multi-point lagrangian velocity estimates. In *Topical Problems of Fluid Mechanics*, 2018.

[28] M. La Mantia and L. Skrbek. Quantum turbulence visualized by particle dynamics. *Physical Review B*, 90(1):014519, 2014.

[29] M. La Mantia. Particle trajectories in thermal counterflow of superfluid helium in a wide channel of square cross section. *Physics of Fluids*, 28(2):024102, 2016.

[30] M. La Mantia, P. Švančara, D. Duda, and L. Skrbek. Small-scale universality of particle dynamics in quantum turbulence. *Physical Review B*, 94(18):184512, 2016.

[31] N. Mordant, E. Lévêque, and J.-F. Pinton. Experimental and numerical study of the lagrangian dynamics of high reynolds turbulence. *New Journal of Physics*, 6:116–116, 2004.

[32] G. W. Stagg, N. G. Parker, and C. F. Barenghi. Superfluid boundary layer. *Physical Review Letters*, 118(13):135301, 2017.

[33] H. Schlichting and K. Gersten. *Boundary-Layer Theory*. Springer, 2017.

[34] S. Babuin, M. Stammeier, E. Varga, M. Rotter, and L. Skrbek. Quantum turbulence of bellows-driven ^{4}He superflow: Steady state. *Physical Review B*, 86(18):184503, 2012.

[35] M. La Mantia. Particle dynamics in wall-bounded thermal counterflow of superfluid helium. *Physics of Fluids*, 29(6):065102, 2017.